Green Synthesis and Catalysis xxx (xxxx) xxx

Contents lists available at ScienceDirect

Green Synthesis and Catalysis

journal homepage: www.keaipublishing.com/en/journals/green-synthesis-and-catalysis

Efficient toluene degradation using *Bacillus subtilis* biofilm-supported Mn–Ce/zeolite catalysts

Muhammad Zubair Mohsin [a,1], Ali Mohsin [a,1,**], Waqas Qamar Zaman [b], Xiaojuan Zhu [a], Xihua Zhao [c], Zain Abbas [d], Muhammad Hammad Hussain [a], Ali Shan [e], Salim-ur-Rehman [f], Muhammad Asif Nawaz [g], Rabia Omer [a], Yingping Zhuang [a], Meijin Guo [a], Jiaofang Huang [a,c,*]

[a] *State Key Laboratory of Bioreactor Engineering, East China University of Science and Technology, Shanghai 200237, China*
[b] *Institute of Environmental Sciences and Engineering, School of Civil and Environmental Engineering, National University of Sciences and Technology (NUST), Islamabad 44000, Pakistan*
[c] *College of Life Science, Jiangxi Normal University, Nanchang 330022, China*
[d] *School of Resources and Environmental Engineering, State Environmental Protection Key Laboratory of Environmental Risk Assessment and Control on Chemical Process, East China University of Science and Technology, Shanghai 200237, China*
[e] *College of Materials Science and Engineering, Shenzhen Key Laboratory of Polymer Science and Technology, Guangdong Research Center for Interfacial Engineering of Functional Materials, Shenzhen University, Shenzhen 518055, China*
[f] *Department of Food Science and Technology, Riphah International University Faisalabad Campus, Faisalabad 44000, Pakistan*
[g] *Institute of Materials Science of Seville (ICMS), University of Seville, Seville 41092, Spain*

ARTICLE INFO

Keywords:
Zeolite
Toluene oxidation
Engineered *Bacillus subtilis* biofilm
Metal nanoparticles
CO_2 selectivity

ABSTRACT

This study investigated a new approach for synthesizing *Bacillus subtilis* biofilm-supported Mn–Ce/zeolite catalysts for the degradation of gaseous toluene. Four different metal oxide nano-catalysts (ZMn, ZMnCe-10%, ZMnCe-20%, and ZMnCe-30%) were synthesized with varying ratios of manganese (Mn) and cerium (Ce) on zeolite nanoparticles. TEM, SEM, XRD, BET, XPS, and EDX mapping were used to examine these four samples, as well as simple zeolite. Based on these analyses, the catalytic activity of the prepared samples ZMn, ZMnCe-10%, ZMnCe-20%, and ZMnCe-30% for the complete oxidation of toluene and toluene intermediate products were tested with Non-thermal plasma (NTP) technology in a dielectric barrier discharge (DBD) reactor. Among all, ZMnCe-20% showed the highest toluene degradation efficiency (89%) at low concentrations (200 ppm) and humidity (>50%). Later, highly efficient and hydrophobic nano-biocatalysts were prepared by combining *B. subtilis* biofilm wild-type (WT) and engineered *B. subtilis* biofilm EPS with ZMnCe-20% catalyst. EPS is the main component found in biofilm matrix and plays a key role in influencing properties such as biofilm stability, electron transfer, surface roughness and hydrophobicity. Compared to WT *B. subtilis* biofilm, EPS overexpressed *B. subtilis* biofilm showed stronger growth and development on ZMnCe-20% nanocatalyst. Moreover, the NTP system packed with ZMnCe-20%/biofilm (EPS+) nano-biocatalyst exhibited the highest toluene degradation activity (99%) with (83%) CO_2 selectivity, (up to 50%) reduction in NOx concentration and complete ozone decomposition at (250 ppm) toluene concentrations and increased humidity (>90%). High-energy electrons generated in the NTP system break the C–H and C–C bond between the rings of the toluene molecule, forming several byproducts which are later reacted with active radical species such as $O^{\bullet}$, $OH^{\bullet}$, and O_3 and further converted into final degradation products (CO_2 and H_2O). The results demonstrated successful biofilm development and growth on the ZMnCe-20% catalyst with advanced features such as superhydrophobicity, H_2O resistance, improved surface roughness, and electron generation. In short, the study's approach combines bioengineering and material science to develop sustainable nano-biocatalysts for removing VOCs in industrial and environmental settings.

* Corresponding author. State Key Laboratory of Bioreactor Engineering, East China University of Science and Technology, Shanghai 200237, China.
** Corresponding author.
E-mail addresses: alimohsin@ecust.edu.cn (A. Mohsin), huangjf@ecust.edu.cn (J. Huang).
[1] Muhammad Zubair Mohsin and Ali Mohsin contributed equally to this work.

https://doi.org/10.1016/j.gresc.2024.01.006
Received 30 November 2023; Received in revised form 23 January 2024; Accepted 24 January 2024
Available online xxxx

Please cite this article as: M.Z. Mohsin et al., Efficient toluene degradation using *Bacillus subtilis* biofilm-supported Mn–Ce/zeolite catalysts, Green Synthesis and Catalysis, https://doi.org/10.1016/j.gresc.2024.01.006

1. Introduction

The emission of toxic volatile organic compounds (VOCs) from industrial sources has been increasing continuously, exceeding the emission control standard limit of 60 mg/m^3 [1,2], and polluting the air quality, posing a serious threat to the ecosystem [3]. Inhaling these toxic compounds from industrial and human-made organic products and chemicals increases the risk of short and long-term adverse health effects [4,5]. Toluene, a major toxic VOC compound, is widely used as a solvent in industries such as paint, dye, textile, and fertilizer. However, the direct release of toluene into the air is considered one of the most dangerous air pollutants [6,7], and it has been designated as a hazardous chemical by the EPA [8,9]. Inhalation of toluene can result in respiratory depression, headaches, fatigue, hallucinations, nausea, dizziness, and other adverse effects, even at low levels [10,11]. Respiratory diseases and lung cancer are highly associated with long-term exposure to toluene emissions from industrial sources [12–16].

In recent years, scientists have turned to zeolite for the remediation of toluene due to its high adsorption efficiency, low cost, and excellent mechanical stability [17,18]. Zeolite nanoparticles (NPs) with low cost have gained much attention due to their hydrophobic properties, active pore system, and ability to catalyze oxidation reactions [19,20]. Zeolite NPs exhibit excellent chemical and physical features [21] and are applied as an absorbent, catalyst, and carrier for microbes for toluene degradation activity [22]. Metals deposited on zeolite NPs coupled with non-thermal plasma (NTP) technology are emerging as a promising strategy for the catalytic oxidation of toluene [23,24]. NTP technology generates highly energetic electrons with reactive particle species (•OH and O• free radicals) that collide with toluene molecules on the catalyst surface initiating the degradation of toluene or converting it into another less toxic by-product at room temperature [25].

Noble metals deposited on zeolite NPs have demonstrated full toluene degradation [26,27]. However, the high cost and rare availability of noble metals restrict their commercial applicability. Therefore, several deposited transition metals (Co, Cu, Fe, *etc.*) on zeolite surface have been proven to be cost-effective and efficient catalysts in the oxidation of toluene under the NTP system [28–32]. Among the most active metal oxides tested on clinoptilolite, manganese (Mn) was found to be highly effective and durable [33]. Several reports have documented the catalytic properties of Mn metal oxides deposited on zeolite NPs for the catalytic oxidation of toluene [24,34]. The abundance of lattice oxygen species on the surface of Mn-supported zeolite plays a major role in the oxidation of toluene molecules [35]. Although several experimental strategies have been carried out on toluene oxidation by Mn-deposited zeolite NPs coupled with the NTP system, the complete degradation of toluene at high concentrations and humidity remains a challenge. Sometimes, during the degradation of toluene, ozone is formed as a byproduct and is unable to be degraded by Mn metal [36]. Therefore, nanostructured CeO_2, as a low-cost catalyst, has been taken into consideration due to its excellent ozonation activity. Ce oxide in the form of (Ce^{4+}/Ce^{3+} pairs) plays a key role in the generation of the hydroxyl radicals that can store and release oxygen in the ozonation activity [26,37,38].

Metal-supported zeolite-based catalysts are highly regarded for their high surface area, and excellent mechanical and thermal stability, and are considered for the adsorption and degradation of toluene. However, one of the significant drawbacks of zeolite catalysts is their low resistance to H_2O vapors, which is attributed to the hydrophilic nature of zeolite [39]. The hydrophilic behavior of zeolite is not only associated with the Si/Al ratio in the structure but also with the binders and H_2O content, which are expected to block pore channels [40]. Guillemot *et al.* [41] found that water vapors negatively influenced the adsorption capacity of zeolites. Under higher humidity conditions, the toluene conversion rate began to decrease, and the catalyst slowly deactivated due to the blockage of active pores, mainly by H_2O molecules [34].

The external surface and cavities of some zeolites contain both acid–base sites. These sites form stronger bonds with H_2O vapors, leading to a reduction in the adsorption of toluene molecules. Additionally, a significant cluster of H_2O is sometimes formed on the surface of zeolite silanol groups due to hydrogen bonding, which significantly reduces or even blocks the transfer of toluene molecules into zeolite pores [42]. Therefore, several researchers have proposed the idea of coating the zeolite surface with a hydrophobic material, which provides resistance against the water molecules blocking the active sites.

In this context, *Bacillus subtilis* (*B. subtilis*), an industrial biofilm-forming bacterium, has gained attention due to its remarkable viscoelastic, hydrophobic, and electroactive properties [43–46]. The biofilm surface of *B. subtilis* can prevent H_2O, solvents, and liquids, making it useful as a hydrophobic agent in the production of hydrophobic building materials [47–49]. Recently, bacterial biofilm was grown on Fe-modified zeolite grains as biocomposites for the degradation of herbicide MCPA (2-methyl-4-chlorophenoxyacetic acid), and it was found to be an effective and stable biocomposite for pesticide biodegradation when treated in both soil and sand [44]. The biofilm-forming *B. subtilis* bacterium is also considered an electrochemically active microorganism (EAM) [50] capable of expressing both intracellular and extracellular electron transfer (IET and EET) functions in the biofilm membrane for respiratory action and energy generation. These electroactive properties have the potential to transfer electrons from intracellular membranes to extracellular electron acceptors, such as minerals and electrodes, thereby increasing the generation of hydroxyl radicals for certain catalytic activities [45]. The two main components involved in the formation of biofilm are extracellular polysaccharides (EPS) and TasA protein [51]. EPS provides mechanical stability to the biofilm and contributes to its formation and adhesion to the surface [52]. EPS is mainly composed of polysaccharides that exhibit electric characteristics of the biofilm due to the presence of several acidic materials, such as uranic acids and ketal-linked pyruvates. EPS also acts as an electron transfer medium and promotes the generation of hydroxyl radicals by the catalyst, accelerating the mineralization reaction [53]. In the global biotech sector, advances in *B. subtilis* biofilms for the development of living materials have grown remarkably in recent years. For example, programmable biofilm-derived biosensors and biotherapeutic agents have been synthesized by using 3D printing technology for their practical applications in the biomaterial industry [54,55]. Previously, in our group, Huang *et al.* [54] provided insight into the engineering of the useful protein TasA with synthetic biology tools to control the functional activity of *B. subtilis* biofilm. These genetic engineering tools have opened doors for the modification of *B. subtilis* biofilms for further applications and prospects.

Primarily, the current work focuses on the construction of a novel, efficient, economical, and highly stable nano-biocatalyst for the mineralization of toluene, toluene intermediate products, and ozone. Furthermore, this study presents an alternative approach to conventional physical, chemical, and biological therapies for the degradation or reduction of toluene toxicity. It also addresses the challenges associated with complex modern 3D architectural constructs and noble metals, as they have demonstrated full toluene degradation. However, the complex synthesis process of these catalysts, and high cost restrict their commercial applicability for removing VOCs in industrial and environmental settings. The study aims to synthesize zeolite-based metal catalysts entrapped in engineered *B. subtilis* biofilms with excellent toluene removal activity and stability under wet conditions. Different samples of Mn–Ce/zeolite nano-catalyst were prepared by loading appropriate % wt of Mn and Ce on zeolite NPs using the wet impregnation method and tested in a DBD reactor to analyze their catalytic activity for toluene oxidation as per the method described in a previous study [56]. In the second part of the study, an EPS overexpression strain 2569 Δ*tasA*Δ*sinR* was constructed and coupled with the synthesized nano-catalyst to check the toluene removal activity with the NTP system. The main objective of this study was to synthesize an inexpensive and highly active nano-biocatalyst with novel approach using combined features and applications of zeolite as an adsorbent material for the adsorption of toluene. Whereas, Mn and Ce NPs were used for the ozone enhanced deep

catalytic oxidation of toluene and toluene intermediates, along with engineered *B. subtilis* biofilms which showed water repulsion activity. Moreover, this engineered biofilm acts as an electron transfer medium and promotes the generation of hydroxyl radicals by the catalyst, accelerating the mineralization reaction exhibiting complete toluene degradation activity compared to the expensive noble metal-based catalyst.

2. Results and discussion

2.1. Characterization of Mn–Ce/zeolite nano-catalysts

The composition of all Mn–Ce/zeolite nano-catalysts was determined using different characterization techniques and described in detail with supporting data, respectively. In order to determine the distribution and content of elements in the synthetic Mn–Ce/zeolite nano-catalysts, SEM and TEM analysis were carried out and illustrated in Fig. 1. As shown in Fig. 1a, zeolite NPs are observed as a flat sheath-like structure with a homogeneous surface providing a large number of active sites for toluene oxidation reactions. Fig. 1b shows changes in zeolite surface morphology after loading Mn NPs. Clusters that appeared on the surface of the zeolite indicated that Mn NPs are well distributed on the zeolite sheath. Fig. 1c and d illustrates that 20 wt% Ce and 30 wt% Ce NPs were loaded successfully onto the Mn-zeolite composite changing the morphology of the Mn-zeolite surface. Numerous spots appeared on the surface of Mn-zeolite after the loading of 20 wt% Ce NPs. When the ratio of Ce NPs was increased to 30 wt%, further denser spots appeared and all the catalysts showed serious agglomeration of Mn and Ce NPs on the surface of the porous zeolite.

It was noted in the TEM image of pure zeolite as shown in Fig. 1e that the extensive dense porous domain existed on the flat sheath surface. After the deposition of Mn, the zeolite sheath showed the better dispersion of Mn NPs denoted by red circles confirming that they are successfully loaded on the surface of zeolite, as shown in Fig. 1f. Then, the addition of Ce to Mn-zeolite gave rise to a prominent influence on the nano-catalyst structure. As shown in Fig. 1g and h, blue arrows indicate that dark spots were highly dispersed on the Mn-zeolite surface as it was difficult to observe the active pores since they were covered after the addition of the 20 wt% Ce ratio increased to 30 wt%. This leads to the conclusion that Ce NPs were dispersed to a great extent on the nanoparticle surface with small particle sizes of 10–20 nm. As all the Mn–Ce/zeolite nano-catalysts showed serious agglomeration of Mn and Ce NPs on the zeolite surface, it was difficult to differentiate Mn and Ce NPs in high-resolution TEM images, which was in agreement with the recently documented study [57]. Therefore, the presence of all elements in the synthetic Mn–Ce/zeolite nano-catalysts was confirmed with SEM-EDX mapping.

Fig. 2 demonstrates SEM-EDX mapping of the synthesized ZMnCe-20% catalyst. The mapping revealed large quantities of Mn and Ce NPs covering the surface of zeolite, confirming a good, homogeneous dispersion of Mn and Ce on the surface. Additionally, microscopic studies revealed the presence of oxygen (O) throughout the zeolite surface. It can be concluded that these highly reactive oxygen species play an important role in the degradation reaction of toluene and ozone, and also contribute to improving the reaction time. The loaded Mn and Ce NPs resulted in the appearance of abundant micropores in Mn–Ce/zeolite nano-catalyst, which was in accordance with the result of N_2 adsorption-desorption isotherm.

The Brunauer–Emmett–Teller (BET) method was used to measure the S_{BET} of the samples. Manganese modification on zeolite increased the S_{BET} to a certain extent. Cerium impregnation further increased the S_{BET} of Mn-zeolite (6.7256 m^2/g) compared to simple zeolite at 0.2174 m^2/g. Among the different cerium-impregnated samples, Mn-Zeolite/20% Ce showed the highest S_{BET} at 8.9666 m^2/g compared to Mn-zeolite, Mn-Zeolite/10% Ce (2.0395 m^2/g), and Mn-Zeolite/30% Ce (3.8102 m^2/g), as shown in Fig. 3a. The study concluded that increasing the content of CeOx on Mn-zeolite might block the pores or disturb the crystalline structure of the parent catalyst [34].

The isotherms of the synthesized materials showed a type II in the Brunauer, Deming, Deming, and Teller (BDDT) classification, which is typical of microporous materials. Mn-zeolite and Mn-Zeolite/20% Ce exhibited excellent pore volume at 0.026102 cm^3/g and 0.021456 cm^3/g, respectively, resulting in improved adsorption performance of the catalyst compared to Mn-Zeolite/10% Ce (0.005130 cm^3/g) and Mn-Zeolite/30% Ce (0.008090 cm^3/g), as shown in Fig. 3b.

The XRD patterns of the zeolite (Z), ZMn, ZMnCe-10%, ZMnCe-20%, and ZMnCe-30% were observed in Fig. 3c. All the catalysts exhibited the

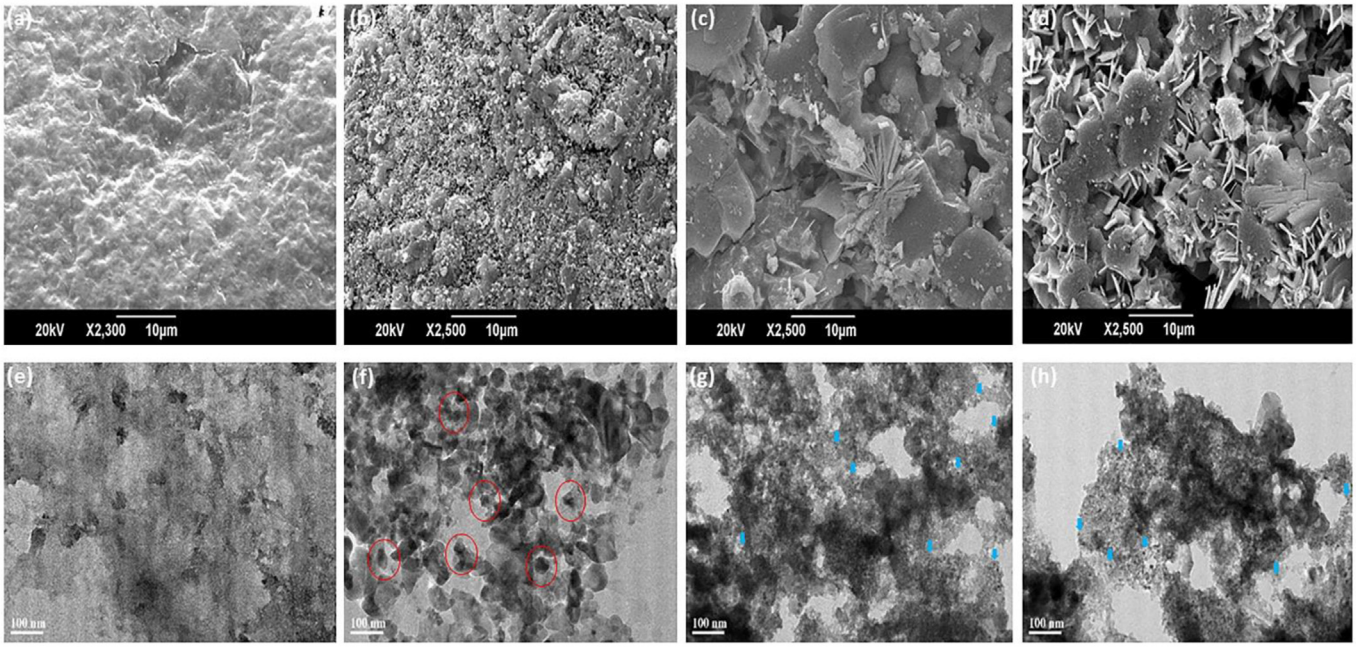

Fig. 1. SEM and TEM images of synthesized samples; (a, e) zeolite, (b, f) Mn loaded zeolite (red circles), (c, g) 20% addition of Ce to Mn-zeolite (blue arrows), (d, h) 30% addition of Ce to Mn-zeolite (blue arrows).

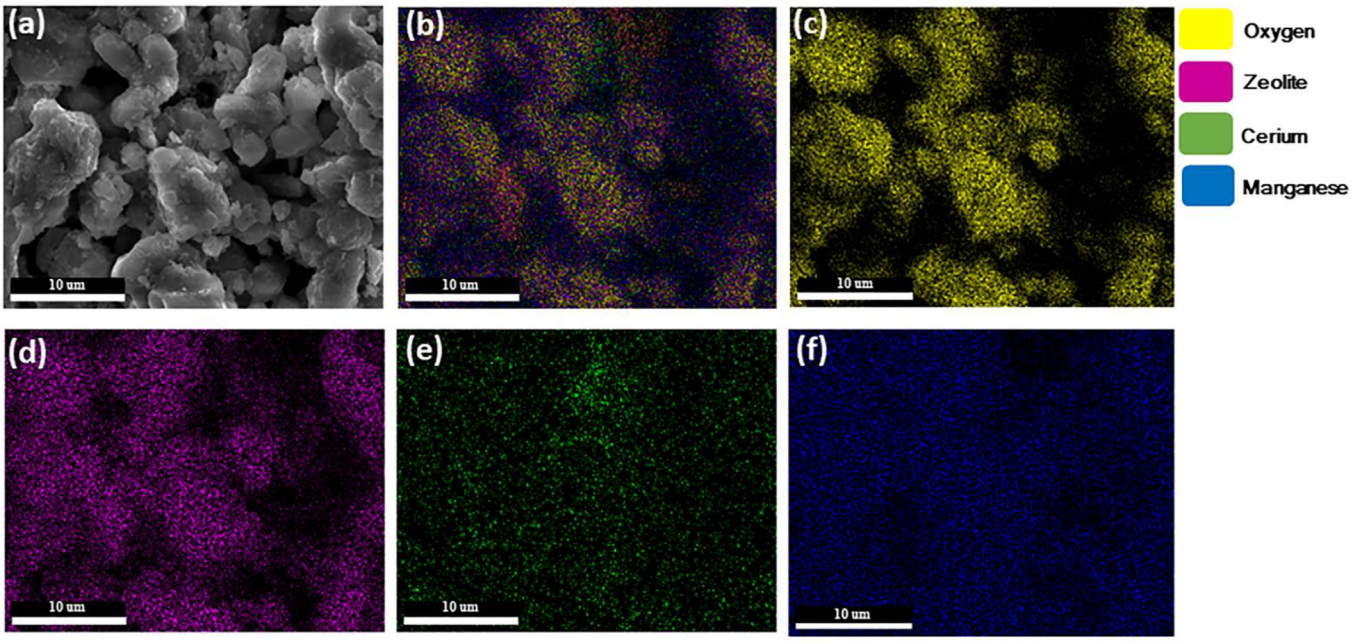

Fig. 2. EDX mapping of synthesized ZMnCe-20%. SEM image (a) and EDX mapping showed aggregated NPs (b) with elements such as oxygen (c), zeolite (d), cerium (e) and manganese (f) were analyzed.

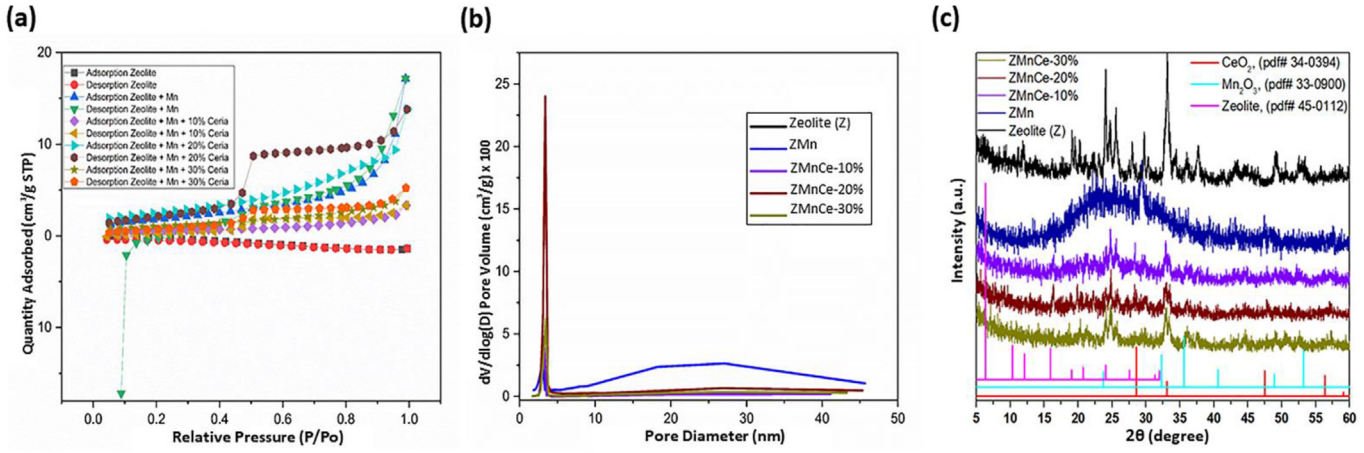

Fig. 3. (a) N_2 adsorption–desorption isotherms (b) pore size distribution and (c) XRD patterns of the zeolite (Z) (black), ZMn (navy), ZMnCe-10% (blue), ZMnCe-20% (brown) and ZMnCe-30% (green) in the panel showing zeolite (purple) corresponding to (pdf# 45-0112), Mn_2O_3 (turquoise) corresponding to (pdf# 33-0900), CeO_2 (red) corresponding to (pdf# 34-0394).

typical pattern of zeolite, with diffraction peaks appear at $2\theta = 10.3°$, 12°, 15.9°, 19.02°, 20.7°, 24.07°, 27.5°, 31.3° and 31.9° and were found to be in good agreement with the data of (pdf# 45-0112) confirm that zeolite was present in all prepared catalysts. The incorporation of Mn and Ce on zeolite via the wet impregnation method retained similar characteristic peaks of the zeolite, indicating that the impregnation method did not damage the structure of the zeolite. Only, the peak intensity for zeolite decreased after the deposition of Mn and Ce content. In the case of zeolite + Mn, the diffraction peaks of Mn_2O_3 were observed at $2\theta = 23.7°$, 32.2°, 35.5°, 40.6°, 49.9°, 53.2°, 62.2° and 64.1° indicating the presence of zeolite and Mn in prepared samples 2–5. XRD peaks of Mn_2O_3 were found to be in good agreement with the data of (pdf# 33-0900). In the case of (Z + Mn + 10% Ce), (Z + Mn + 20% Ce), and (Z + Mn + 30% Ce), the diffraction peaks of CeO_2 were observed at $2\theta = 28.5°$, 33.8°, 47.4°, 56.3°, 69.4° and 76.6° indicating the presence of Ce in prepared samples 3–5, corresponding to the data of (pdf# 34-0394).

The chemical compositions and oxidation states of the prepared samples, including zeolite, ZMn, ZMnCe-10%, ZMnCe-20%, and ZMnCe-30%, were investigated using X-ray photoelectron spectroscopy (XPS). The results showed that all samples clearly exhibited the presence of elements, including zeolite, Mn, Ce, and oxygen species. The spectrum of the Si 2p region for zeolite displayed a clear spin-orbit splitting peak, and the peak at approximately 102.45 eV in all samples confirmed the presence of zeolite.

Furthermore, the spectrum of the Mn 2p region for manganese presence in samples (ZMn, ZMnCe-10%, ZMnCe-20%, and ZMnCe-30%) showed clear spin-orbit splitting peaks, and the peaks at 641.38, 642.28, 645, 647.66, 655.03, and 653.38 eV. The Mn 2p spectrum peaks indicated the existence of Mn^{3+} as well as Mn^{4+}, which is in line with previously documented reports [58,59]. Similarly, the spectrum of the Ce 3d 5/2 region for cerium displayed clear double spin-orbit splitting peaks, and the peaks at 882.51, 885.60, 887.54, and 898.28 were consistent with previous literature [60]. The spectrum of the Ce 3d 3/2 region for

cerium also displayed clear double spin-orbit splitting peaks, and the peaks at 901.23, 904.39, 907.37, and 916.63 eV. Moreover, v0, v1 in the Ce 3d5/2 region, and v0′, v1′, v2′ in Ce 3d3/2 region represent Ce^{3+}. Similarly, u0, u1 in the Ce 3d5/2 region, and u1′ in the Ce 3d3/2 region represent Ce^{4+}. The XPS results indicated the coexistence of Ce^{3+} and Ce^{4+} in the synthesized catalyst (ZMnCe-10%, ZMnCe-20%, and ZMnCe-30%), which is expected to play a key role in the decomposition of O_3 into hydroxyl radicals and other reactive species. The atomic ratios of zeolite in sample 1 and Mn^{3+}, Mn^{4+} in sample 2 and Ce^{3+}, Ce^{4+} in sample 3–5 have been shown in Fig. 4.

Similarly, the atomic ratio of adsorbed/lattice oxygen species (O 1s) of all the samples (1–5) has been mentioned in Fig. S1 in Supporting information for details. All the atomic ratios of the samples have been identified by curve fitting procedure as mentioned in Table 1 were highly present in ZMnCe-30% (4.96) and ZMnCe-20% (4.65). From O 1s XPS spectra, two kinds of oxygen species such as lattice oxygen and adsorbed oxygen were identified. The high valence content of metals results in the increased holding of adsorbed oxygen content and reactivity potential.

Fig. S2 in Supporting information for details illustrates the H_2-TPR analysis of the catalysts utilized in the current study. The reduction peak of ZMn was first detected at 620 °C. With the addition of 10% Ce, the reduction peak of ZMnCe-10% was shifted towards a higher temperature. However, 20% Ce was found to be the optimal amount to add as it exhibited the strongest reducibility power, with the reduction peak beginning at 390 °C. No significant improvement in reducibility power was observed with further increases in the amount of Ce, as evidenced in the case of ZMnCe-30%. The broader reduction peak of ZMnCe-20%, compared to ZMn, ZMnCe-10%, and ZMnCe-30%, is attributed to its higher reduction power, which is linked to its better oxidation activity.

The SEM, TEM, and XRD analyses confirmed the presence of zeolite, Mn, and Ce in all samples, which is consistent with previous studies [34, 58–60]. ZMnCe-20% displayed the highest S_{BET} and reducibility compared to the other catalysts, while the atomic ratios for Mn, Ce, and oxygen species were higher in ZMnCe-30% than in ZMnCe-20% when calculated using curve fitting procedures. These findings suggest that while ZMnCe-30% had higher atomic ratios for Mn, Ce, and oxygen species, it had the lowest S_{BET}, resulting in a decreased number of active pores for the adsorption of toluene molecules, ultimately affecting the toluene oxidation activity.

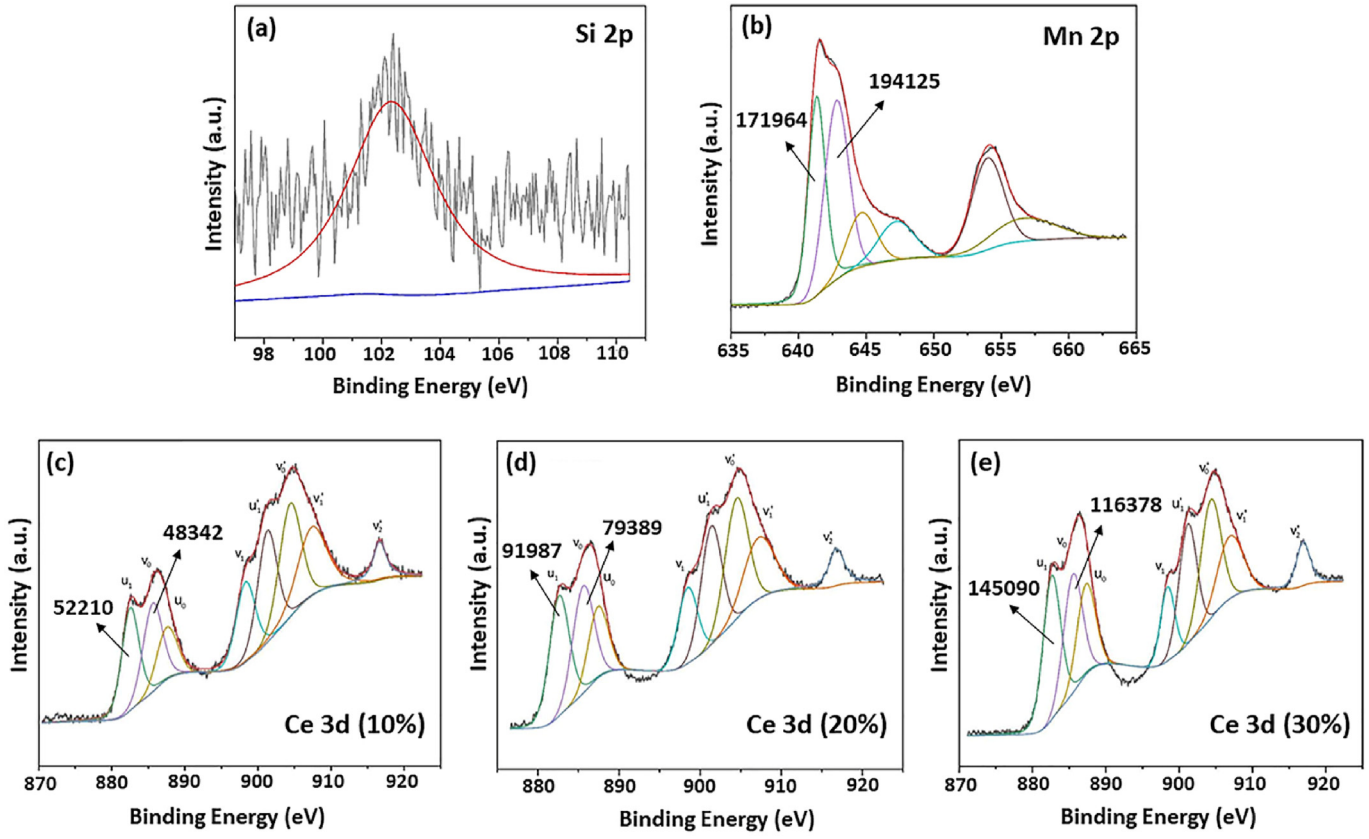

Fig. 4. (a) Spectrum of Si 2p region for zeolite, (b) Mn 2p region for manganese display and atomic ratios of Mn^{3+} and Mn^{4+}, (c) Spectrum of Ce 3d 3/2 region for cerium display and atomic ratios of Ce^{3+} and Ce^{4+}, (d) Spectrum of Ce 3d 3/2 region for cerium display and atomic ratios of Ce^{3+} and Ce^{4+}, (e) Spectrum of Ce 3d 3/2 region for cerium display and atomic ratios of Ce^{3+} and Ce^{4+}.

Table 1
The % ratio of Mn oxides, Ce oxides and oxygen species (lattice oxygen and adsorbed oxygen) was calculated from zeolite (Z), ZMn, ZMnCe-10%, ZMnCe-20%, ZMnCe-30% catalysts using XPS measurements.

Catalyst	Mn^{3+} B.E. (eV)	Mn^{4+} B.E. (eV)	Mn^{3+}/Mn^{4+}	Ce^{3+} B.E. (eV)	Ce^{4+} B.E. (eV)	Ce^{3+}/Ce^{4+}	$O_{adsorbed}$ B.E. (eV)	$O_{lattice}$ B.E. (eV)	$O_{adsorbed}/O_{lattice}$
Zeolite (Z)	–	–	–	–	–	–	159794.6	291976.2	0.54
ZMn	171964	194125	0.88	–	–	–	814238	231969	3.51
ZMnCe-10%	171964	194125	0.88	52210	48342	1.080	590795.1	201158.1	2.93
ZMnCe-20%	171964	194125	0.88	91987	79389	1.158	764206.2	164252.1	4.65
ZMnCe-30%	171964	194125	0.88	145090	116378	1.246	781998.9	157353	4.96

2.2. Catalytic evaluation of synthesized Mn–Ce/zeolite nano-catalysts with NTP system

The experiment began with the oxidation of toluene in the NTP setup alone, where the catalytic activity of the system was investigated in the absence of the catalyst. Plasma was generated in the NTP system, which converted most of the electrical energy into highly energetic electrons. By increasing the input energy, the production of high-energy electrons, free radicals, ions, and other particles increased, leading to even more intense collisions between electrons, which further increased the number of reactions and boosted toluene removal efficiency [61].

Under NTP conditions, toluene is more smoothly destroyed than other VOCs due to the weak C–C bond between CH_3 and C_6H_5 fragments, which is in agreement with the documented study [62]. Another theoretical study also affirms the distribution of various species (electrons or active radicals) in the NTP system due to the abundant generation of methyl radicals during the decomposition of toluene. Such radicals boost toluene degradation activity by promoting some reactions such as the decomposition of intermediate o-benzoquinone, giving rise to several new reaction pathways resulting in the generation of new unpredicted toxic intermediates [63]. HO_2, CH_4, H_2O, and benzyl radicals ($C_6H_5CH_2$) are generated in a plasma reactor via H-abstraction reactions which are able to react further with OH resulting in the formation of benzyl alcohol and benzaldehyde [64]. Furthermore, the subsequent reaction of benzyl radicals could be responsible for the combination and activation of toluene molecules [65]. Therefore, direct toluene degradation in the DBD reactor failed to achieve significant efficiency and resulted in the production of O_3 as well as several toxic by-products.

In the initial series of systematic experiments, the catalytic activity and selectivity of four different synthesized nano-catalysts (ZMn, ZMnCe-10%, ZMnCe-20%, and ZMnCe-30%) with the NTP system were carried out in the DBD reactor at room temperature. Toluene molecules along with several toxic intermediates were adsorbed on the nano-catalysts' active sites. The generated free radical species such as $O^{\bullet}$, $OH^{\bullet}$, and O_3 react with cyclic substances on the surface of nano-catalysts which further react with the ring substances to break the ring, resulting in the generation of acids, esters, amides and long-chain alkanes. Further reactions on nano-catalysts surface between the high-energy electrons, radical species, and excited molecules, resulted in the degradation of toluene and toluene intermediates into several small metabolites such as CO_2, H_2O, O_3 and NOx [66]. The best toluene degradation efficiency was observed by ZMnCe-20% at 54 W (89%) at an initial toluene concentration of 200 ppm, and the CO_2 selectivity was greater than 65%. The degradation efficiency decreased with an enhanced initial toluene concentration of 250 ppm and high humidity of 90%. However, the degradation efficiency could be balanced at a level of 87% by increasing the energy efficiency, as shown in Fig. 5a, and a slight decrease in CO_2 selectivity was noted. CO_2 selectivity is important for evaluating the performance of plasma-assisted catalyst systems in toluene oxidation treatment. Higher CO_2 selectivity means a higher mineralization rate of VOCs. The toluene degradation ranking for all the synthesized catalysts in this study is as follows: ZMnCe-20% > ZMn > ZMnCe-30% > ZMnCe-10% > NTP alone. Toluene removal efficiency (TRE) and CO_2 selectivity were calculated by using the formula:

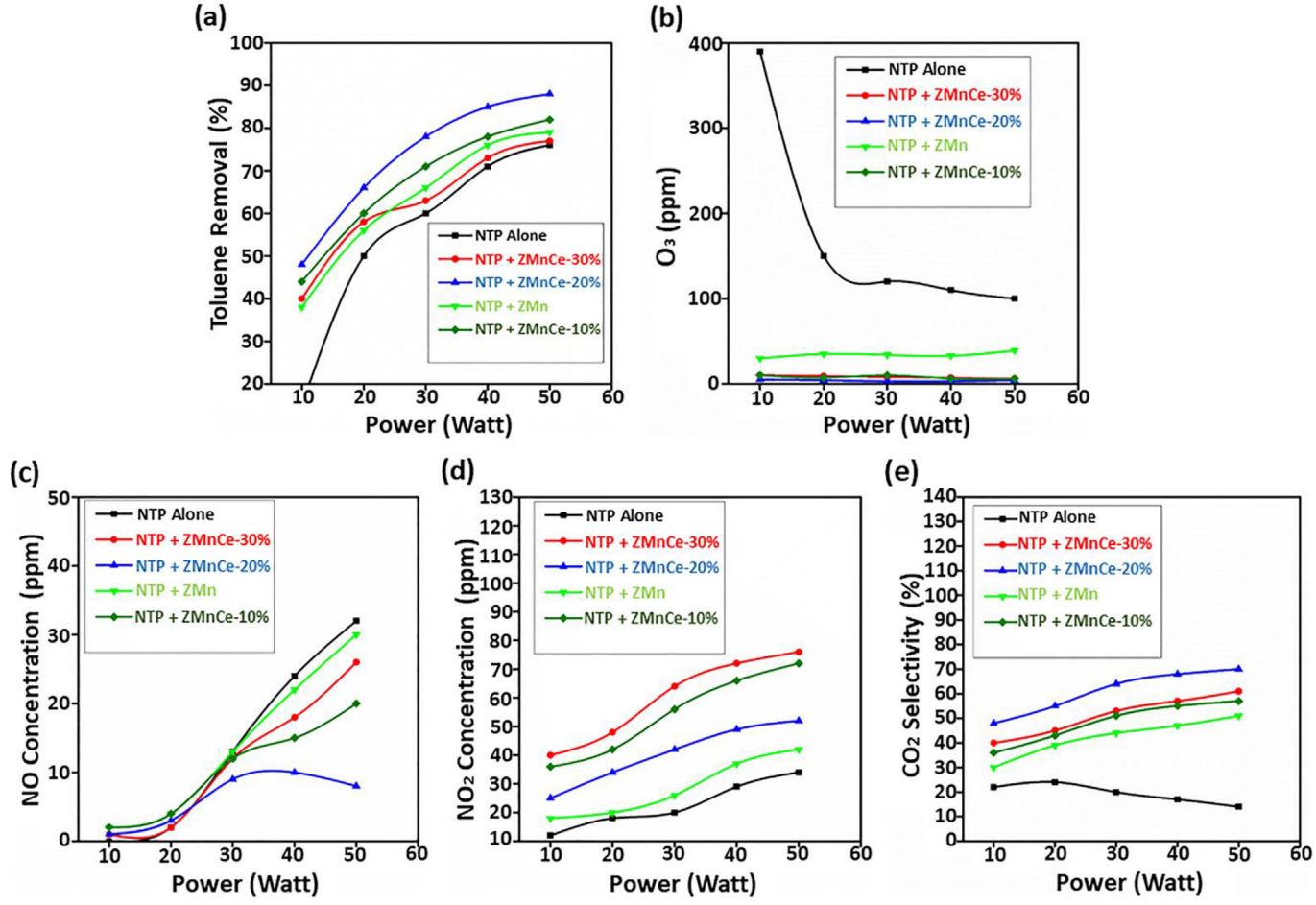

Fig. 5. (a) Toluene degradation efficiency, (b) Ozone decomposition, (c and d) NOx (NO and NO_2) reduction and (e) CO_2 selectivity of nano-catalysts (ZMn, ZMnCe-10%, ZMnCe-20% and ZMnCe-30%) combined with NTP technology.

Where C_{in} and C_{out} are the inlet and outlet concentrations of toluene, respectively, while (CO_2) represents the amount of CO_2 monitored from the outlet.

$$\text{Toluene removal} = \frac{[C_7H_8]_{in} - [C_7H_8]_{out}}{[C_7H_8]_{in}} \times 100\% \quad (1)$$

$$CO_2 \text{ selectivity} = \frac{CO_2}{7(C_7H_8)_{in} - (C_7H_8)_{out}} \times 100\% \quad (2)$$

The increased O_3 removal in the system is another benefit of the NTP system packed with nano-catalysts. The O_3 concentration in the NTP system without catalysts was noted at a high level >100 ppm even when the input energy increased. Because the O_3 produced in the NTP system plays a key role in the catalytic oxidation of toluene, when the NTP is coupled with the synthesized nano-catalyst, O_3 is eliminated. Notably, the hydroxyl radical and oxygen radicals created by the breakdown of ozone were the active oxygen species that first caused the degradation of toluene to begin. Compared to ZMn and NTP alone, ZMnCe-10%, ZMnCe-20%, and ZMnCe-30% exhibited total ozone elimination, as shown in Fig. 5b. Based on the ozone removal results, the high ratio of Mn^{3+}/Mn^{4+}, Ce^{3+}/Ce^{4+}, and OA/OL ratio of catalysts ZMnCe-10%, ZMnCe-20%, and ZMnCe-30% were taken into consideration for the excellent catalytic activity [67].

During toluene oxidation, NOx is formed as an unfavorable byproduct. In the NTP system, when the input energy is high, Nitrogen (N_2) molecules break down into nitrate N radicals, which react with atomic oxygen and oxygen radicals to generate NO_2. This can affect the toluene degradation reaction rate and even lead to the deactivation of the catalyst. However, the synthesized catalyst showed significant suppression of NOx in the NTP system. The addition of O_3 to flue gas in the ozone treatment produced even more promising results as NO formed during combustion was completely oxidized to NO_2. Moreover, the NO produced at low input energy could not be detected in the system because it reacts with O_3 and produces NO_2 [68]. All the prepared catalysts, especially ZMnCe-20%, showed promising results for toluene degradation, with a significant reduction in NOx concentration (lower than 10% for NO and 50% for NO_2) compared to NTP alone, as shown in Fig. 5c and d.

In terms of CO_2 selectivity, the order was ZMnCe-20% > ZMnCe-30% > ZMn > ZMnCe-10% > NTP alone. The ZMnCe-20% catalyst with the NTP system exhibited the maximum toluene degradation efficiency and CO_2 selectivity (>65%), as shown in Fig. 5e, due to its large surface area and the greater number of active sites that lead to maximum adsorption of toluene molecules inside the cavities. This was correlated with SEM, TEM, and BET results, as well as with the high Mn^{3+}/Mn^{4+}, Ce^{3+}/Ce^{4+} and adsorbed/lattice oxygen ratio mentioned in Table 1. By increasing the input energy to 54 W, the toluene degradation efficiency reached 87%, concluding that high energetic electrons play an important role in toluene removal. Oxygen-active species (hydroxyl radical and oxygen radical) formed on the surface of the catalyst as a result of O_3 decomposition. Several intermediates formed during the oxidation of toluene were further oxidized to CO_2 by oxygen-active species, which contributed to the enhancement of CO_2 selectivity.

The NTP system alone showed around 70% degradation of toluene but also produced around 20 hazardous byproducts identified by GC–MS chromatogram of the organic byproducts in this experiment. This is consistent with previous reports documenting the production of byproducts in the NTP system alone [66,69]. Continuous formation of these byproducts limits the toluene oxidation application of the NTP system. However, coupling NTP with synthesized catalysts generates active species that promote the degradation of toluene and hazardous byproducts, as shown in Table S1 in Supporting information for details. Most of the byproducts were not observed after the introduction of catalysts in the experiment. Benzene, benzonitrile, formic acid, benzyl alcohol, benzoic acid and benzaldehyde were the main toluene intermediates identified by GC–MS chromatogram with and without the ZMnCe-based nano-catalysts and are considered to be more toxic than toluene. These intermediates are generated in relevant abundance during the toluene degradation activity indicating the breaking and formation of chemical bonds or occurrence of other oxidation-reduction reactions between molecules in order to produce new unpredicted toxic intermediates which are consistent with previous documented studies [63,70]. Interestingly, by increasing the humidity in the system, the production of some of the unpredicted toxic intermediates is hindered. This complex reaction mechanism is attributed to the noble metal-based catalytic studies [71,72], which reported that H_2O vapors may react with intermediates during the toluene degradation pathway which might ascribe to the base-catalyzed hydrolysis of ester bonds, inhibiting the formation of some unpredicted intermediates and lead the toluene degradation pathway to the direct generation of benzoic acid.

Maximum degradation of toluene requires high-energy electrons generated in the NTP system. These electrons and N_2 excited states (A3, a') directly breakdown the C–H and C–C bond between the methyl and benzene ring of the toluene molecule, forming benzyl and phenyl compounds as byproducts. These byproducts further react with active radical species such as $O^{\bullet}$, $OH^{\bullet}$, and O_3 to produce benzyl alcohol, benzaldehyde, benzoic acid, etc. which are later converted into final degradation products (CO_2 and H_2O).

The synthesized catalyst, especially ZMnCe-20%, achieves high oxidation of toluene but byproducts such as benzene, benzaldehyde, formic acid, benzyl alcohol, benzoic acid and benzonitrile were detected with the increase in toluene concentration and high humidity, thus limiting the deep oxidation of toluene. However, under the increased humidity conditions, the production of several unexpected toxic toluene intermediates was considered to be suppressed [71] but the toluene conversion rate began to decrease. This is because increased H_2O vapors form stronger bonds with acid–base sites on zeolite and easily adsorbed than toluene, even forming a cluster of H_2O on zeolite silanol groups, blocking the adsorption of toluene molecule into active pores [34,42].

All samples were assessed in the NTP system to determine their activity for the deep catalytic oxidation of toluene. ZMnCe-20% exhibited the highest toluene degradation activity (89%) with complete ozone decomposition and reduced NOx concentrations compared to ZMn, ZMnCe-30%, ZMnCe-10%, and NTP alone. Additionally, the CO_2 selectivity was higher in ZMnCe-20% (>65%). These findings suggested that adsorption played a crucial role in the degradation activity of toluene. However, with an increase in humidity, there was a slight decrease in toluene oxidation performance, which could be adjusted to 87% by controlling the energy efficiency. Nonetheless, CO_2 selectivity started to decline as toluene intermediate products failed to convert to CO_2 and H_2O, potentially because water vapors competed with toluene molecules on adsorption sites by blocking the active pores. As a result, the zeolite-based metal catalyst failed to achieve complete deep oxidation of toluene and toluene intermediate products at high humidity. The stability of ZMnCe-20% catalyst during catalytic degradation of toluene was also assessed at 250 ppm concentration and >50% humidity. It was observed that toluene degradation proceeded stably during the first 9 h for ZMnCe-20% at room temperature. Afterwards, the degradation of toluene started to decrease as shown in Fig. S3. Thus, further synthesis of catalysts with hydrophobic characteristics, increased stability, and catalytic activity is required.

To improve the hydrophobicity and catalytic activity of the nano-catalyst in highly humid conditions, we used two biofilm strains, *B. subtilis* wild-type strain 2569 and EPS overexpression strain 2569*ΔtasAΔsinR* (EPS+), coupled with ZMnCe-20% due to their excellent toluene removal performance. After the entrapment experiment, the two obtained nano-catalysts, ZMnCe-20%/biofilm (WT) and ZMnCe-20%/biofilm (EPS+) were characterized by SEM, TEM, and FT-IR to analyze the surface morphology and confirm the successful entrapment of nano-catalysts in both biofilms.

2.3. Characterization of Mn–Ce/zeolite nano-catalyst in natural and engineered B. subtilis biofilms

The SEM and TEM images of the biofilms-coated Mn–Ce/zeolite nano-catalyst are presented in Fig. 6. The SEM images clearly show that an encapsulating layer covers the NPs, which range from approximately 700-800 nm. Additionally, EPS overexpressed *B. subtilis* biofilm exhibits thicker coverage on ZMnCe-20%, as shown in Fig. 6a than wild-type *B. subtilis* biofilm, as shown in Fig. 6b. The SEM images of the surface texture of the nano-catalyst also suggest a higher roughness for ZMnCe-20%/biofilm (EPS+).

The presence of nano-catalyst entrapped in *B. subtilis* biofilm was further confirmed by TEM images. The engineered *B. subtilis* biofilm covered more catalyst surface, as shown in Fig. 6c compared to wild-type *B. subtilis* biofilm, as shown in Fig. 6d. The presence of strong biofilm formations and enlargement in the ZMnCe-20%/biofilm (EPS+) sample confirmed the role of EPS in biofilm formation. The construction of EPS overexpression strain 2569ΔtasAΔsinR (EPS+) also confirmed similar results of strong biofilm formation activity with increased surface roughness and hydrophobic characteristics compared to the wild-type strain.

FTIR spectroscopy was used to analyze changes in the *B. subtilis* biofilm matrix when exposed to a ZMnCe-20% catalyst. The analysis aimed to determine whether the NPs induced any changes in the biofilm components. The IR spectra for ZMnCe-20%/biofilm (WT) and ZMnCe-20%/biofilm (EPS+) samples showed first peaks in the range of 950–1000 cm^{-1} wave number and a second peak in the range of 1140–1200 cm^{-1} wave number, confirming the presence of components such as nucleic acids, polysaccharides, and phospholipids. The stretching mode of the C═O bond was displayed at a wavenumber of 1655 cm^{-1}, while the N–H bond deformation mode combined with the stretching mode of C–N was displayed at a wavenumber of 1534 cm^{-1}. Additionally, a large peak at a wavenumber of 3200–3500 cm^{-1} showed amide N–H stretching in the *B. subtilis* biofilm, as demonstrated in Fig. S4 in Supporting information for details, which is consistent with previous studies [73,74]. The three peaks in each sample did not change, indicating that the components of the biofilm were not affected by the synthesized nano-catalyst ZMnCe-20%. Although the formation and dispersal of biofilm increased, the expansion of the peaks varied between the two samples.

2.4. Characteristics evaluation of Mn–Ce/zeolite catalyst entrapped in B. subtilis biofilm in DBD reactor

The successful entrapment of Mn–Ce/zeolite in biofilms was confirmed by SEM and TEM analysis of both ZMnCe-20%/biofilm (WT) and ZMnCe-20%/biofilm (EPS+) samples. The engineered *B. subtilis* biofilm covered more catalyst surface compared to wild-type *B. subtilis* biofilms. The strong biofilm formation and enlargement in the ZMnCe-20%/biofilm (EPS+) sample confirmed the role of EPS in biofilm formation. Furthermore, FT-IR results confirmed the presence of biofilm components (nucleic acids, polysaccharides, and phospholipids), indicating that the ZMnCe-20% nano-catalyst did not affect the composition of the biofilm. In order to check the improved hydrophobic and catalytic activity, both samples were tested in DBD and evaluated for performance.

In a second series of catalytic activity tests, systematic experiments for the two new biofilm-based catalysts, ZMnCe-20%/biofilm (WT) and ZMnCe-20%/biofilm (EPS+), were carried out in a DBD reactor to test their catalytic activity. The highest toluene degradation efficiency at 50 W was observed (99%) for ZMnCe-20%/biofilm (EPS+) and (94%) for ZMnCe-20%/biofilm (WT) at an increased concentration of toluene (250 ppm) as shown in Fig. 7a. The catalyst activity of ZMnCe-20%/biofilm (EPS+) was stable even at high humidity (>90%), indicating excellent water resistance ability as the biocatalyst showed increased surface roughness and hydrophobicity observed in SEM analysis. The super-hydrophobic surface of the biofilm blocks the water molecules to compete with the toluene molecules for adsorption on active sites, resulting in the availability of more active sites for toluene and maximum adsorption. Moreover, EPS acts as a chief electron transport mediator on the surface of the catalyst, enhancing the production and transport of high active oxygen species (superoxide oxygen species) between the active sites through biofilm bridging, boosting the toluene catalytic oxidation reaction.

Complete degradation of ozone was achieved with both prepared samples, ZMnCe-20%/biofilm (WT) and ZMnCe-20%/biofilm (EPS+), during the toluene degradation experiment in the NTP system. This is because the degradation of toluene was initiated by the reaction with active oxygen species, such as hydroxyl radicals and oxygen radicals produced from ozone degradation. Additionally, at high input energies, ozone and NO react to generate NO_2. Therefore, highly active species in

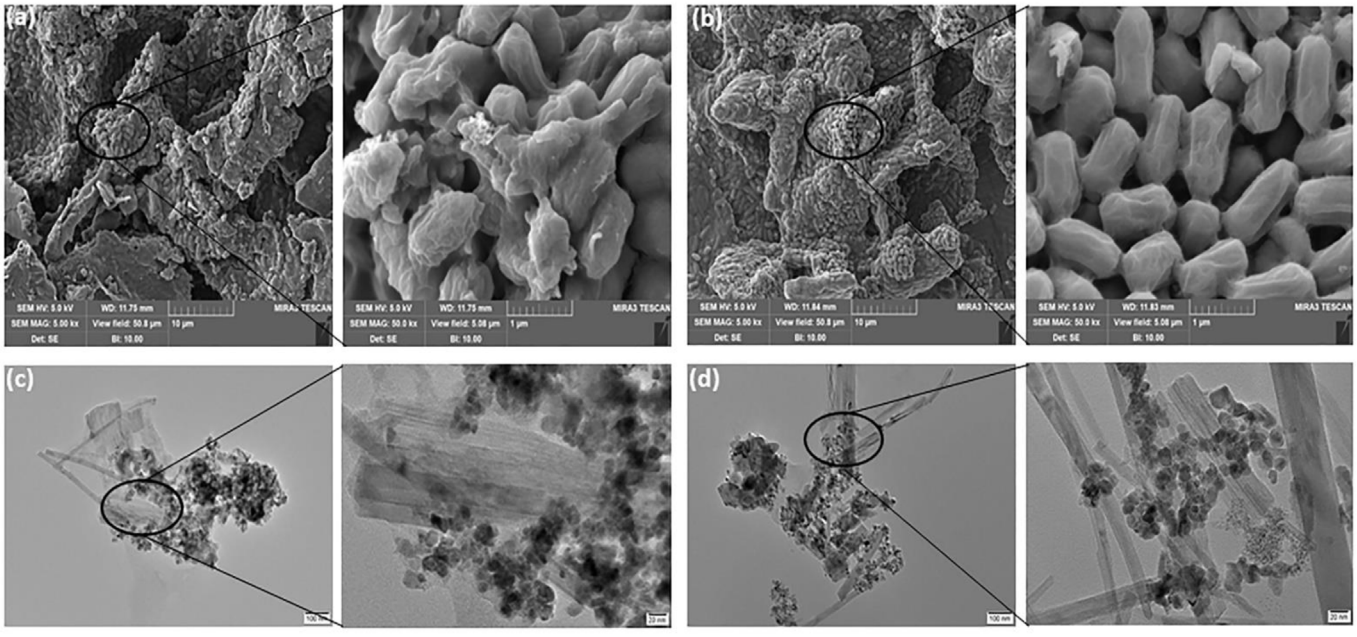

Fig. 6. (a and c) SEM and TEM images of ZMnCe-20%/biofilm (EPS+), (b and d) SEM and TEM images of ZMnCe-20%/biofilm (WT) samples showing nano-catalyst entrapped in biofilm.

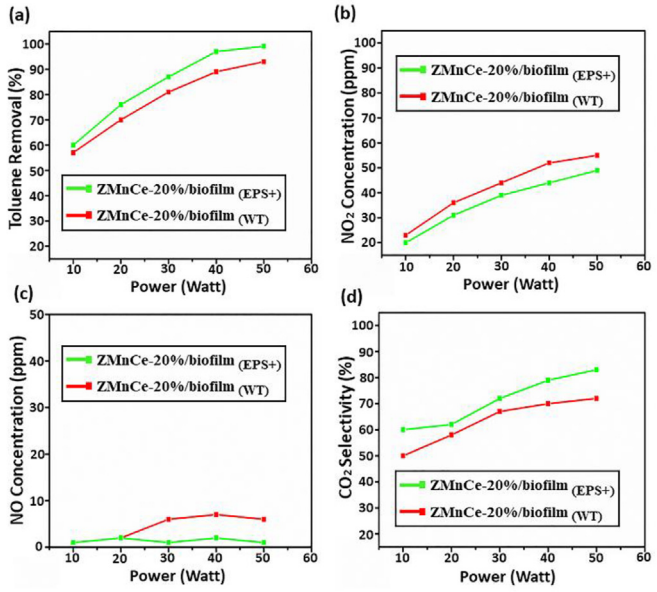

Fig. 7. (a) Toluene mineralization efficiencies, (b and c) NOx (NO and NO_2) reduction and (d) CO_2 selectivity by *B. subtilis* biofilm entrapped nano-catalysts ZMnCe-20%/biofilm (WT) and ZMnCe-20%/biofilm (EPS+).

the system breakdown the N_2 radical into N, which was later reacted with atomic oxygen and oxygen radicals to form NO_2, which was slightly reduced by both *B. subtilis* biofilm-entrapped catalysts, lower than 60% with ZMnCe-20%/biofilm (WT) and lower than 50% with ZMnCe-20%/biofilm (EPS+), as shown in Fig. 7b and c.

After adding the developed *B. subtilis* biofilm-based biocatalyst, the complete oxidation of toluene and the decomposition of ozone increased significantly, leading to increased CO_2 selectivity. Moreover, the residual intermediate products of toluene, such as benzaldehyde, formic acid, acetic acid, benzene, and benzonitrile, were completely oxidized to CO_2 and H_2O in the NTP system treated with ZMnCe-20%/biofilm (EPS+). This indicates the high generation activity of reactive oxygen species on the biocatalyst surface, prompted by EPS *B. subtilis* biofilms. Both ZMnCe-20%/biofilm (WT) and ZMnCe-20%/biofilm (EPS+) produced CO_2 selectivity of 70% and 83%, respectively, as shown in Fig. 7d. The stability of ZMnCe-20%/biofilm (EPS+) during catalytic degradation of toluene was also assessed at 250 ppm concentration and increased humidity >90%. It was observed that toluene degradation proceeded stably during the first 12 h for ZMnCe-20%/biofilm (EPS+). After that, the degradation of toluene started to decrease as shown in Fig. S5. Overexpressed *B. subtilis* biofilm strain (EPS+) demonstrated excellent resistance against oxidative stress under NTP conditions. This is due to the presence of abundant Mn oxides in the developed nano-catalyst which play an important role in upsurging *B. subtilis* biofilm development [75, 76]. Another promising factor is the increased level of humidity that could be responsible for the generation of additional OH radicals as biofilm undergoes several physiological changes under NTP conditions. During the mineralization reaction, ZMnCe-20% catalyst utilized these additional OH radicals with the help of EPS in the biofilm which plays a key role as an electron transfer medium between the active sites of the catalyst through biofilm bridging [53]. Although, experimental difficulty in examining the biofilm activity under the complex NTP system has limited our understanding regarding the role of water-biofilm interaction in this fundamental aspect. Therefore, to understand this mechanism, several factors during water-biofilm interaction could be taken into consideration for the generation of additional OH radical species. In general, biofilms comprise over 70 wt% water and bacteria in biofilms are actively involved in building water-filled structures for cellular functions. The surface of biofilm is hydrophobic and have the ability to resist external water molecules in air at the gas–liquid interface. Although bacteria need external water for its growth, therefore, the edges of biofilm are hydrophilic in nature and can absorb water on the biofilm matrix surface which is considered as bound water and can be used for purposes such as cell signaling and nutrients transfer under physiological stresses or immune responses [77].

3. Conclusion

In conclusion, the proposed research work presents a novel approach for synthesizing an eco-friendly, cost-effective, and highly efficient zeolite-based catalyst by entrapping different ratios of metal oxides in engineered *B. subtilis* biofilm. The first part of the study focused on developing zeolite-based metal catalysts using different ratios of Mn and Ce metal oxides for the complete oxidation of toluene and its intermediate products. ZMnCe-20% showed the greatest toluene degradation efficiency (87%) when evaluated using NTP technology at high humidity levels, but CO_2 selectivity was only 65% due to poor wettability resistance. In the second part of the study, the highly efficient and hydrophobic biocatalysts were developed by combining the ZMnCe-20% catalyst with *B. subtilis* biofilms, resulting in ZMnCe-20%/biofilm (WT) and ZMnCe-20%/biofilm (EPS+). The ZMnCe-20%/biofilm (EPS+) biocatalyst demonstrated maximum toluene degradation activity (99%) and excellent ozone decomposition with 83% CO_2 selectivity, even at high humidity and increased toluene concentrations. The biofilm played a crucial role as an electron transport mediator in the oxidation of toluene, while the catalyst's enhanced hydrophobicity and surface roughness prevented H_2O vapors from competing with toluene molecules for adsorption on the catalyst's active sites. Our study presents a promising solution for the complete deep oxidation of toluene and its intermediate products in high-humidity environments. Our zeolite-based biocatalyst with *B. subtilis* biofilm is more economical and highly effective than other synthetic catalysts, making it a viable alternative for industrial applications.

Overall, the conducted study has opened new avenues for the synthesis of efficient and economical nano-biocatalysts for the degradation of toluene. However, there are still challenges that need to be addressed to make this approach more practical and effective. One major challenge is NOx reduction which was not achieved in the end. This was due to the high-energy reaction between NO and O to produce NO_2, which proved challenging for the catalyst to effectively decrease following ozone decomposition. Furthermore, all the experiments have been conducted at lab-scale for specific pollutants (toluene). The efficiency of nano-biocatalyst could be affected by the presence of multiple pollutants generated in the real industrial sectors. Therefore, further studies are required to explore the fate of other VOCs, and mineralization of all the possible byproducts as well as to analyze the efficiency of nano-biocatalysts at a commercial scale.

4. Materials and methods

4.1. Chemicals, microbes, biofilm preparation

4.1.1. Chemical, microbes and reagents

All reagents and chemicals used in this research work were of analytical grade. Natural clinoptilolite zeolite was purchased from Sigma Aldrich (USA), Merck (DE), Acros Organics (Thermo Fischer Scientific, USA) or Prolabo (France). *B. subtilis* strain 2569 was a kind gift from Professor Daniel Kearns (Indiana University, the USA).

4.1.2. Biofilm preparation

4.1.2.1. Construction of B. subtilis EPS over expression strain 2569ΔtasAΔsinR. In this presented study, the construction of EPS over-expression strain 2569Δ*tasA*Δ*sinR* (EPS+) was performed according to

our previous study of Huang et al. [54]. To create Δ*tasA*Δ*sinR* mutant strain, we first constructed a suicide plasmid, pMAD-Δ*tasA*Δ*sinR*, which has a 2-Kb fragment (with tasAsinR deletion) inserted into a plasmid named pMAD. Then the plasmid pMAD-Δ*tasA*Δ*sinR* was transformed into *B. subtilis* 2569 WT strain, and the fragment (Δ*tasA*Δ*sinR*) was integrated into the genome to generate a *B. subtilis* 2569Δ*tasA*Δ*sinR* mutant.

The transformed strain was selected on an LB erythromycin agar plate, and incubated at 30 °C. Selective transformants were then re-streaked onto nonselective LB, grown overnight at 42 °C. Isolates were patched onto LB agar having 5 μg/mL of erythromycin. PCR fragments from the mutant's genomic DNA were sequenced to confirm the removal of the *tasAsinR* gene.

4.1.2.2. Biofilm cultivation. B. subtilis wild-type strain 2569 and EPS overexpression strain 2569 Δ *tasA* Δ *sinR* (EPS+) were grown into 5 mL LB broth (1% trypsin (Difco), 0.5% yeast extract (Difco) and 1% NaCl) at 37 °C with shaking at 220 rpm overnight. Then it was transferred into 100 mL LB medium according to 1% inoculation amount, and when its cell density reached $OD_{600} = 4$, it was centrifuged at 5000 rpm for 5 min at room temperature and resuspended in MSgg medium which provided carbon and energy for biofilm formation at 30 °C static culture for 2–3 days. Biofilm was collected, wild-type strain 2569 and overexpression EPS strain 2569Δ*tasA*Δ*sinR* being noted as *B. subtilis* biofilm (WT) and *B. subtilis* biofilm (EPS+), respectively and then further used in entrapment experiment with prepared catalyst.

4.2. Catalyst preparation

4.2.1. Mn–Ce/zeolite nano-catalyst preparation

Mn–Ce/zeolite nano-catalysts were synthesized using the conventional wet impregnation method. Firstly, 1 g of oven-dried zeolite was taken in a dry china dish. Deionised (DI) water was added dropwise to determine how much water the zeolite can adsorb. 0.7 mL of DI water was enough to fully wet the zeolite material. Then, 5 g of oven-dried zeolite was taken in a clean dry china dish. 2.28 g of manganese nitrate tetrahydrate ($Mn(NO_3)_2{\cdot}4H_2O$) were dissolved in 3.5 mL of DI water (based on the determined adsorption capacity in the previous step). Four such replicates were prepared. This solution was added dropwise over the zeolite in the china dish. The resulting mixture was left at room temperature for 12 h. Then the mixture was oven-dried at 105 °C for 12 h. Finally, the mixture was calcined in a muffle furnace at 400 °C for 6 h. The resulting material from one china dish was put in an Eppendorf tube for analysis. The remaining three mixtures of the previous step were taken in 3 different china dishes. 155 mg, 310 mg and 465 mg of cerium nitrate hexahydrate ($Ce(NO_3)_3{\cdot}6H_2O$) were dissolved in 3.5 mL of DI water each (based on the determined adsorption capacity in the initial step). These solutions were added dropwise to the zeolite-Mn mixture. The purpose of these 3 variations was to add by weight 10%, 20% and 30% of ceria to zeolite. The resulting mixture was left at room temperature for 12 h. Then the mixture was oven dried at 105 °C for 12 h. Finally, the mixture was calcined in a muffle furnace at 400 °C for 6 h. The resulting material was put in three different Eppendorf tubes for analysis.

Conclusively, by following this method we prepared four samples ZMn, ZMnCe-10%, ZMnCe-20% and ZMnCe-30%, respectively. Among these ZMn constitutes just zeolite and manganese oxide; whereas, the other three samples constitute zeolite, manganese oxide and cerium oxide. The numeric digits 10%, 20% and 30% in nomenclature represent % wt of Ce to Mn in all three samples.

4.2.2. Mn–Ce/zeolite nano-catalyst entrapment in B. subtilis biofilm

To assess the nano-catalyst entrapment efficiencies, we exposed *B. subtilis* biofilm (WT) and *B. subtilis* biofilm (EPS+) to the ZMnCe-20% NPs (1:1, v/v), following stirring and mixing using a magnetic stirrer for 3 h. After that, these samples were centrifuged at 12,000 rpm for 30 min, and the pellets were collected and freeze-dried. In these prepared samples, 2 g of fresh biofilm contain 100 mg of ZMnCe-20% NPs. The two obtained samples were noted as ZMnCe-20%/biofilm (WT) and ZMnCe-20%/biofilm (EPS+). The samples were first analyzed to check the successful entrapment of ZMnCe-20% in both biofilm strains and then tested in the DBD reactor to evaluate the toluene removal activity.

4.3. Catalyst characterization

As mentioned above, four different nano-catalysts (ZMn, ZMnCe-10%, ZMnCe-20% and ZMnCe-30%) were prepared using the wet impregnation method. The Brunauer–Emmet–Teller (BET) surface area (S_{BET}) and pore size analysis of ZMn, ZMnCe-10%, ZMnCe-20% and ZMnCe-30% along with parent zeolites (Z) were determined through nitrogen adsorption–desorption isotherms at 77 K using an ASAP 2010 analyzer (Micrometritics Company, America). X-ray diffraction (XRD) analysis was performed with a diffractometer X'TRA (ARL Company, Switzerland) using Cu Kα radiations at 30 kV and 10/min scan speed. The scanning electron microscope (SEM) was conducted to measure the surface microtopography of the sample with an electronic scanning energy spectroscopy instrument (FEI QUANTA FEG250). Transmission electron microscopy (TEM) images were obtained to analyze the internal structure of the samples with a JEM-2100CX microscope (JEOL Ltd., Japan) at 200 kV. The X-ray photoelectron spectra (XPS) analysis was carried out on a PHI 5000 Versa Probe equipment (ULVAC-PHI Ltd., Japan) for the surface chemical studies of all nano-catalysts with monochromatic Al source. All binding energy was corrected by fixing C1s photoelectron peak at 284.6 eV and the collected data were measured through the XPS Peak 4.1 software. Energy dispersive X-ray spectroscopy (EDX) mapping of the nano-catalysts was acquired with Hitachi S-4800FEG scanning electron microscope (SEM) to measure the morphology of the samples. Hydrogen temperature programmed reduction (H_2-TPR) analysis was obtained with Auto Chem 2920 Micromeritics to examine the redox characteristics of understudy catalysts.

In the next series, after the selection of catalyst based on catalytic performance, two nano-biocatalysts noted as ZMnCe-20%/biofilm (WT) and ZMnCe-20%/biofilm (EPS+) were developed by combining engineered nano-catalyst with *B. subtilis* biofilms following the nanoparticle/biofilm entrapment experiment. These two samples were then again characterized by SEM and TEM to analyze the surface morphology to confirm the successful entrapment of nano-catalysts in both of the biofilms. Further, in order to check *B. subtilis* biofilm development and growth, and whether exposure to different NPs induces changes in the matrix components during biofilm formation, samples were characterized by FT-IR spectroscopy analysis using Nicolet (Waltham, MA, USA) 605XR FT-IR spectrophotometer.

4.4. NTP experiment

NTP experiments for catalytic activity tests were conducted in a DBD reactor operated at room temperature and ambient pressure. The scheme of the experimental setup was operated by following the standard method described in the previous study [56]. The apparatus included sections of toluene gas generation, a DBD plasma reactor with a power supply system, a catalyst reactor and gas analyzing instruments. Toluene vapors were generated by introducing nitrogen (N_2) gas through a liquid toluene kept in the water bath at a temperature of 24 ± 1 °C and then sent to the DBD reactor using a Teflon pipe. A mass flow controller was used to regulate the flow of N_2 gas for controlling the initial concentration of toluene diluted with pure air. Then, toluene gas mixed with air was introduced into the reactor at a flow rate of 900 mL/min. In this experiment, a high-voltage AC transformer (CTP-2000K, Suman, Nanjing, China) supplied a high alternating-current (AC) power in series. Varied input powers (10 W, 20 W, 30 W, 40 W and 50 W) were applied to generate plasma with an AC power of 220 V at 50 Hz. The mass of ZMn, ZMnCe-10%, ZMnCe-20%, ZMnCe-30%, ZMnCe-20%/biofilm (WT) and ZMnCe-20%/biofilm (EPS+) used were all 0.5 g, placed in a catalytic

reactor. In the initial phase, the toluene concentration was adjusted to around 200 ppm and then increased to 250 ppm in order to check the performance efficiency and stability of the nano-catalysts. Toluene was determined using a gas chromatograph (GC9890A, Shanghai, China) equipped with a flame ionization detector (FID). Potential toluene intermediates formed with and without catalysts were identified using gas chromatography–mass spectroscopy (GC–MS). A humidity meter (Center 310, Shuangxu, Shanghai, China) was employed to measure humidity. CO_2 concentration in the system was measured by a CO_2 detector (GXH-3010E, Huayun, Beijing, China), respectively. O_3 detector (DCS-1, Lida, Shanghai, China) was used to determine O_3 concentration. NOx concentration in the system was monitored with a NOx monitoring analyzer (Model 42i, Thermo Fisher Scientific, USA).

CRediT authorship contribution statement

Muhammad Zubair Mohsin: Writing – review & editing, Writing – original draft, Visualization, Validation, Methodology, Formal analysis, Data curation, Conceptualization. **Ali Mohsin:** Writing – review & editing, Writing – original draft, Supervision, Methodology, Funding acquisition, Formal analysis, Data curation. **Waqas Qamar Zaman:** Validation, Resources, Methodology, Investigation, Formal analysis, Data curation. **Xiaojuan Zhu:** Validation, Methodology, Formal analysis, Data curation. **Xihua Zhao:** Methodology, Data curation. **Zain Abbas:** Methodology, Investigation. **Muhammad Hammad Hussain:** Methodology, Investigation. **Ali Shan:** Resources. **Salim-ur-Rehman:** Methodology, Investigation. **Muhammad Asif Nawaz:** Methodology, Investigation. **Rabia Omer:** Methodology. **Yingping Zhuang:** Supervision, Resources. **Meijin Guo:** Resources, Project administration. **Jiaofang Huang:** Writing – review & editing, Supervision, Project administration, Methodology, Investigation, Funding acquisition, Conceptualization.

Declaration of competing interest

The authors declare that they have no known competing financial interests or personal relationships that could have appeared to influence the work reported in this paper.

Acknowledgments

This research work was supported by the National Key Research and Development Program of China (No. 2020YFA0908900), the National Natural Science Foundation of China (No. 22250410275), the Natural Science Foundation of Shanghai (No. 22ZR1416000) and also by the Fundamental Research Funds for the Central Universities.

Appendix A. Supplementary data

Supplementary data to this article can be found online at https://doi.org/10.1016/j.gresc.2024.01.006.

References

[1] G. Liu, W. Xi, X. You, Y. Zhi, C. Li, IOP Conf. Ser. Earth Environ. Sci. 227 (2019) 062037.
[2] D. Jing, N. Cheng, C. Zhang, Z. Chen, X. Cai, S. Li, J. Zhao, Q. Wang, W. Li, J. Environ. Sci. 121 (2022) 25–37.
[3] E. David, V.C. Niculescu, Int. J. Environ. Res. Public Health 18 (2021) 13147.
[4] T.Z. Maung, J.E. Bishop, E. Holt, A.M. Turner, C. Pfrang, Int. J. Environ. Res. Public Health 19 (2022) 8752.
[5] X. Zhou, X. Dong, R. Ma, X. Wang, F. Wang, J. Hazard. Mater. 416 (2021) 125827.
[6] G. Pelletti, F. Rossi, M. Garagnani, R. Barone, R. Roffi, S. Mater. 416 (2021) 125827.
[7] C. Sayles, N. Finnegan, T. Pike, M.W. Spence, Toxicol. Ind. Health 38 (2022) 606–621.
[8] S.R. Clough, in: P. Wexler (Ed.), Toluene, Academic Press, Oxford, 2014, pp. 595–598.
[9] Z.W. Mo, H. Niu, S.H. Lu, M. Shao, B. Gou, Huan jing ke xue 36 (2015) 1944–1951.
[10] C.M. Filley, W. Halliday, B.K. Kleinschmidt-Demasters, J. Neuropathol. Exp. Neurol. 63 (2004) 1–12.
[11] S.L. Cruz, M.T. Rivera-García, J.J. Woodward, J. Drug, Alcohol Res. 3 (2014) 235840.
[12] R.M. Park, Saf. Health Work 12 (2021) 174–183.
[13] H. Warden, H. Richardson, L. Richardson, J. Siemiatycki, V. Ho, J. Occup. Environ. Med. 75 (2018) 696.
[14] S. Kim, E. Park, S.H. Song, C.W. Lee, J.T. Kwon, E.Y. Park, B. Kim, Environ. Int. 146 (2021) 106304.
[15] A. Aasi, S.M. Aghaei, B. Panchapakesan, Nanotechnology 31 (2020) 415707.
[16] A.M. Ahmed, A. Mehaney, H.A. Elsayed, Eur. Phys. J. Plus 136 (2021) 626.
[17] T. Xue, L. Yang, Front. Chem. 9 (2021) 751581.
[18] L. Xu, Y. Li, J. Zhu, Z. Liu, Trans. Tianjin Univ. 25 (2019) 312–321.
[19] A. Vaezihir, M.B. Bayanlou, Z. Ahmadnezhad, G. Barzegari, J. Contam. Hydrol. 230 (2020) 103604.
[20] F. Sher, A. Hazafa, T. Rashid, M. Bilal, F. Zafar, Z. Mushtaq (Eds.), Biodegradation and biodeterioration, at the nanoscale, Elsevier., 2022, pp. 579–601.
[21] A. Khaleque, M.M. Alam, M. Hoque, S. Mondal, J.B. Haider, B. Xu, M.A.H. Johir, A.K. Karmakar, J.L. Zhou, M.B. Ahmed, M.A. Moni, Environ. Adv. 2 (2020) 100019.
[22] Z. Ahmadnezhad, A. Vaezihir, C. Schüth, G. Zarrini, Chemosphere 273 (2021) 128555.
[23] X. Zhang, B. Ren, Y. Xu, X. Li, P. Yu, Y. Sun, H. Zheng, Sep. Purif. Technol. 257 (2021) 117973.
[24] X. Yao, J. Zhang, X. Liang, C. Long, Chemosphere 208 (2018) 922–930.
[25] W. Xu, K. Lin, D. Ye, X. Jiang, J. Liu, Y. Chen, Nanomaterials 9 (2019) 290.
[26] H. Xiao, J. Wu, X. Wang, J. Wang, S. Mo, M. Fu, L. Chen, D. Ye, Mol. Catal. 460 (2018) 7–15.
[27] J. He, D. Chen, N. Li, Q. Xu, H. Li, J. He, J. Lu, Appl. Catal. B Environ. 265 (2020) 118560.
[28] D. Romero, D. Chlala, M. Labaki, S. Royer, J.-P. Bellat, I. Bezverkhyy, J.-M. Giraudon, J.-F. Lamonier, Catalysts (2015) 1479–1497.
[29] H. Yi, X. Yang, X. Tang, S. Zhao, J. Wang, X. Cui, T. Feng, Y. Ma, J. Chem. Technol. Biotechnol. 92 (2017) 2276–2286.
[30] X. Xu, J. Wu, W. Xu, M. He, M. Fu, L. Chen, A. Zhu, D. Ye, Catal. Today 281 (2017) 527–533.
[31] A. Aziz, S. Kim, K.S. Kim, J. Environ. Chem. Eng. 4 (2016) 3033–3040.
[32] A. Aziz, J. Bae, K.S. Kim, Water Air Soil Pollut. 231 (2020) 155.
[33] G.S.P. Soylu, Z. Özçelik, İ. Boz, Chem. Eng. J. 162 (2010) 380–387.
[34] Q. Shao, H. Dong, J. Zhang, B. Xu, Y. Wu, C. Long, Chemosphere 271 (2021) 129604.
[35] Y. Peng, L. Zhang, L. Chen, D. Yuan, G. Wang, X. Meng, F.-S. Xiao, Catal. Today 297 (2017) 182–187.
[36] M. Wu, D.Y.C. Leung, Y. Zhang, H. Huang, R. Xie, W. Szeto, F. Li, Chem. Eng. Sci. 195 (2019) 985–994.
[37] C.A. Orge, J.J.M. Órfão, M.F.R. Pereira, A.M. Duarte de Farias, R.C.R. Neto, M.A. Fraga, Appl. Catal. B Environ. 103 (2011) 190–199.
[38] L. Bo, S. Sun, Front. Chem. Sci. Eng. 13 (2019) 385–392.
[39] P.S. Chintawar, H.L. Greene, Appl. Catal. B Environ. 14 (1997) 37–47.
[40] M. Kraus, U. Trommler, F. Holzer, F.-D. Kopinke, U. Roland, Chem. Eng. J. 351 (2018) 356–363.
[41] M. Guillemot, J. Mijoin, S. Mignard, P. Magnoux, Microporous Mesoporous Mater. 111 (2008) 334–342.
[42] B.S. Bal'zhinimaev, E.A. Paukshtis, A.V. Toktarev, E.V. Kovalyov, M.A. Yaranova, A.E. Smirnov, S. Stompel, Microporous Mesoporous Mater. 277 (2019) 70–77.
[43] Y. Su, C. Liu, H. Fang, D. Zhang, Microb. Cell Factories 19 (2020) 173.
[44] N. Gorodylova, A. Seron, K. Michel, C. Joulian, F. Delorme, C. Soulier, S. Bresch, C. Garreau, F. Giovannelli, C. Michel, Appl. Soil Ecol. 180 (2022) 104614.
[45] Y. Qin, Y. He, Nat. Commun. 10 (2019) 3702.
[46] S. Pandit, M. Fazilati, K. Gaska, Int. J. Mol. Sci. 21 (2020) 6755.
[47] S. Arnaouteli, N.C. Bamford, N.R. Stanley-Wall, Á.T. Kovács, Nat. Rev. Microbiol. 19 (2021) 600–614.
[48] S. Grumbein, D. Minev, M. Tallawi, K. Boettcher, F. Prade, F. Pfeiffer, C.U. Grosse, O. Lieleg, Adv. Mater. 28 (2016) 8138–8143.
[49] S. Arnaouteli, C.E. MacPhee, N.R. Stanley-Wall, Curr. Opin. Microbiol. 34 (2016) 7–12.
[50] N. Eghtesadi, K. Olaifa, F.M. Perna, V. Capriati, M. Trotta, O. Ajunwa, E. Marsili, Bioelectrochemistry 147 (2022) 108207.
[51] S.S. Branda, F. Chu, D.B. Kearns, R. Losick, R. Kolter, Mol. Microbiol. 59 (2006) 1229–1238.
[52] N. Ido, A. Lybman, S. Hayet, D.N. Azulay, M. Ghrayeb, S. Liddawieh, L. Chai, Soft Matter 16 (2020) 6180–6190.
[53] Y. Wang, H. Fan, P. Keung Wong, Y. Wu, B. Rittmann, Bioresour. Technol. 323 (2021) 124638.
[54] J. Huang, S. Liu, C. Zhang, X. Wang, J. Pu, F. Ba, S. Xue, H. Ye, T. Zhao, K. Li, Y. Wang, J. Zhang, L. Wang, C. Fan, T.K. Lu, C. Zhong, Nat. Chem. Biol. 15 (2019) 34–41.
[55] C. Zhang, J. Huang, J. Zhang, S. Liu, M. Cui, B. An, X. Wang, J. Pu, T. Zhao, C. Fan, T.K. Lu, C. Zhong, Mater. Today 28 (2019) 40–48.
[56] L. Sun, W. Luo, W. Sun, J. Yang, Res. Chem. Intermed. 45 (2019) 2903–2913.
[57] J. Xiao, M. Wang, Y. Wang, X. Li, J. He, Y. Liu, Q. Xu, H. Li, N. Li, D. Chen, J. Lu, Ind. Eng. Chem. Res. 61 (2022) 18382–18389.
[58] H. Huang, W. Huang, Y. Xu, X. Ye, M. Wu, Q. Shao, G. Ou, Z. Peng, J. Shi, J. Chen, Q. Feng, Y. Zan, H. Huang, P. Hu, Catal. Today 258 (2015) 627–633.
[59] G. Wu, Y. Gao, F. Ma, B. Zheng, L. Liu, H. Sun, W. Wu, Eng. J. 271 (2015) 14–22.
[60] M. Trudeau, A. Tschöpe, J. Ying, Surf. Interface Anal. 23 (2004) 219–226.
[61] H.T. Quoc An, T. Pham Huu, T. Le Van, J.M. Cormier, A. Khacef, Catal. Today 176 (2011) 474–477.
[62] O. Karatum, M.A. Deshusses, Chem. Eng. J. 294 (2016) 308–315.

[63] Y. Liang, Y. Xue, D. Fang, T. Tan, Z. Jiang, W. Shangguan, J. Yang, Y. Pan, Fundam. Res. (2022), https://doi.org/10.1016/j.fmre.2022.03.026. In press.
[64] M. Pelucchi, C. Cavallotti, T. Faravelli, S. Klippenstein, Phys. Chem. Chem. Phys. 20 (2018) 10607–10627.
[65] L.B. Harding, S.J. Klippenstein, Y. Georgievskii, J. Phys. Chem. A 111 (2007) 3789–3801.
[66] M. Li, D. Li, Z. Zhang, C. Ji, S. Zhou, W. Guo, C. Zhao, F. Liu, F. Han, J. Environ. Chem. Eng. 9 (2021) 105529.
[67] J. Kim, E.E. Kwon, J.E. Lee, S.-H. Jang, J.-K. Jeon, J. Song, Y.-K. Park, J. Hazard. Mater. 403 (2021) 123934.
[68] Y. Guo, X. Liao, M. Fu, H. Huang, D. Ye, J. Environ. Sci. 28 (2015) 187–194.
[69] H. Huang, D. Ye, D.Y.C. Leung, F. Feng, X. Guan, J. Mol. Catal. A: Chem. 336 (2011) 87–93.
[70] H. Fenglei, L. Mengyu, Z. Huangrong, L. Ting, L. Dandan, Z. Shuo, G. Wenwen, L. Fang, J. Saudi Chem. Soc. 24 (2020) 673–682.
[71] F. Bi, S. Ma, B. Gao, Y. Yang, L. Wang, F. Fei, J. Xu, Y. Huang, M. Wu, X. Zhang, Fuel 344 (2023) 128147.
[72] C.F. Cullis, T.G. Nevell, D.L. Trimm, J. Chem. Soc., Faraday Trans. 1: Phys. Chem. Condens. Phases 68 (1972) 1406–1412.
[73] N. Haddad, J. Wang, B.-Z. Mu, Protein Pept. Lett. 16 (2009) 7–13.
[74] W. Ma, D. Peng, S.L. Walker, B. Cao, C.-H. Gao, Q. Huang, P. Cai, npj Biofilms Microbiomes 3 (2017) 4.
[75] E. Mhatre, A. Troszok, A.R. Gallegos-Monterrosa, S. Lindstädt, T. Hölscher, O.P. Kuipers, Á.T. Kovács, Microbiology (Reading, Engl.) 162 (2016) 1468–1478.
[76] M. Sharipova, N. Rudakova, A. Mardanova, V. Evtugyn, Y. Akosah, I. Danilova, A. Suleimanova, Microorganisms 11 (2023) 1486.
[77] K. Quan, J. Hou, Z. Zhang, Y. Ren, B.W. Peterson, H.C. Flemming, C. Mayer, H.J. Busscher, H.C. van der Mei, Crit. Rev. Microbiol. 48 (2022) 283–302.